
Supplementary information

Flexo-photovoltaic effect in MoS₂

In the format provided by the
authors and unedited

1 Supplementary Information

2
3
4
5

Flexo-Photovoltaic Effect in MoS₂

Jiang, J. et al.

| | |
|----|--------------------------------------|
| 6 | Table of Contents |
| 7 | |
| 8 | Supplementary Discussions 1–5 |
| 9 | |
| 10 | Supplementary Figures 1–23 |

11 **Supplementary Discussions**

12 **Supplementary Discussion 1: Shift and ballistic current**

15 The shift current is determined by non-diagonal band elements of the electron-density matrix and can be
16 expressed as^{1,2}

17 $\mathbf{j}_{\text{sh}} = e \sum_{\psi, \psi'} W_{\psi', \psi} \mathbf{R}_{\psi', \psi}, \quad (1)$

18 where e is the elementary charge, $W_{\psi', \psi}$ is the optical transition rate from Bloch state ψ to ψ' , and $\mathbf{R}_{\psi', \psi}$ is the shift vector of electrons in real space that can be described by the Berry connection in momentum space³ (see refs^{1,3-5} for details). The shift current occurs in the atomic-scale relaxation time (about 0.1–1 fs). Recently, theorists have calculated the shift current in ferroelectric materials by first principles calculations⁶⁻⁸ and illustrate that shift current photovoltaics may compete with conventional ones^{9,10}. The ballistic current can be expressed as²

24 $\mathbf{j}_b = -e \sum_{s, k} \mathbf{f}_{s, k} \mathbf{v}_{s, k}, \quad (2)$

25 where $\mathbf{f}_{s, k}$ is the momentum \mathbf{k} distribution in band s and $\mathbf{v}_{s, k}$ is the electron velocity.

27 **Supplementary Discussion 2: Schematics of strain gradient engineering in the MoS₂ sheet**

29 Supplementary Fig. 1a and b show schematics of the side view and top view of the hybrid system MoS₂/VO₂, respectively. Here for clear illustration, a monolayer MoS₂ is used. Due to the geometry of MoS₂ at the edge of VO₂, a lattice expansion of MoS₂ (a change of lattice constant from a_0 to a_1) may be induced, leading to a strain gradient η . When VO₂ undergoes the structural phase transition from M1 phase to R phase with the lattice parameter changing from a_{xM1} to a_{xR} , the lattice parameter of MoS₂ changes from a_1 to a_1' due to the interaction between MoS₂ and VO₂, leading to a modified strain gradient η' , as shown in the side view and top view in Supplementary Fig. 1c and d, respectively. By controlling the structural phase transition of VO₂, this strain gradient in MoS₂ can be tuned. Supplementary Fig. 1e–f show schematics of the shape (Supplementary Fig. 1e) and supercells (Supplementary Fig. 1f,g) of a VO₂ microbeam before (M1 phase, gray) and after (R phase, orange) the phase transition. The as-grown VO₂ microbeam has bounding surfaces of (0̄11), (20̄1) and (011) in M1 phase, which are approximately perpendicular to axes of x , y and z , respectively. Following the naturally formed bounding surfaces, supercells of M1 and R phases are chosen to demonstrate the lattice change. Calculated from the lattice parameters of unit cells in M1 and R phases in the ref.¹¹, the lattice parameters of the supercell a_{xM1} and a_{zM1} are 12.83 Å, a_{yM1} is 5.75 Å, a_{xR} and a_{zR} are 12.87 Å, a_{yR} is 5.70 Å, $\alpha(M1)$ is 89.79°, $\beta(M1)$ is 90.25°, $\gamma(M1)$ is 89.05°, and $\alpha(R)$, $\beta(R)$ and $\gamma(R)$ are 90°. Thus, after the phase transition from M1 to R, the VO₂ lattice parameters along x and z directions have elongations of 0.3%, while the lattice parameter along y direction has a contraction of 0.9%.

48 **Supplementary Discussion 3: Control experiment in strain gradient controlled MoS₂/VO₂**

50 The schematic of the device structure for our control experiment in Supplementary Fig. 7a illustrates our design (transferring MoS₂ on the substrate first followed by the stacking of VO₂ micron beam on it). By stacking the VO₂ microbeam on the MoS₂ sheet, we expect to avoid forming strain gradient but keep the interface of MoS₂/VO₂. This way we expect to rule out the contribution of the strain gradient to photocurrent so we can focus on investigating the contribution of potential gradient resulted from charge transfer/band bending from the MoS₂/VO₂ interface. The optical image in Supplementary Fig. 7b shows our control device. We have performed Raman mapping of E_{2g}^1 mode of MoS₂ on this device, as shown Supplementary Fig. 7c. Indeed, we do **not** find any substantial peak shift of E_{2g}^1 mode. Thus, there is no substantial strain gradient in the MoS₂ sheet. Meanwhile, the short-circuit photocurrent map in Supplementary Fig. 7d only exhibit signals of positive sign. If charge transfer/band bending occurs, we would expect photocurrent signals to have similar magnitude but with opposite signs at both microbeam edges due to the symmetry of

61 our device. Clearly, this is not observed. Therefore, this control experiment suggests that the observed
 62 photocurrents with opposite signs in our experiments of other six devices (where MoS₂ is above VO₂) are
 63 not due to charge transfer/band bending. It is theoretically possible there may be a charge transfer/band
 64 bending between MoS₂ and VO₂ since they are different materials. However, according to our experiment,
 65 the contribution from this is negligible.

66

67 **Supplementary Discussion 4: Repeatability of flexo-photovoltaic (FPV) effect**

68

69 To improve statistics, we have fabricated another five devices with different thicknesses of MoS₂ sheets
 70 and VO₂ microbeams (devices #2–#6 in Supplementary Fig. 8–12a,b,c, respectively). We have repeated the
 71 Raman, short-circuit photocurrent and current-voltage measurements (Supplementary Fig. 8e–g, 9e–g, 10e–
 72 g, 11f,g, 12e–g, Supplementary Fig. 8d,h, 9d,h, 10d,h–j, 11d,e, 12d,h, and Supplementary Fig. 13a,b (device
 73 #3), respectively). The high repeatability of strain gradients, photocurrents and their distributions (among
 74 all devices) and the strong correlation between the photocurrent and strain gradient in all devices indicate
 75 that our experimental observation of the FPV effect in MoS₂ is a universal effect. Despite different
 76 thicknesses and uniformity of the MoS₂ sheets among all devices (it is noted that FLGs overlap VO₂ in
 77 devices #1, #2 and #6, not in devices #3, #4 and #5), the experimental observations of strain gradient and
 78 its relation to photo currents are similar.

79

80 **Supplementary Discussion 5: Linear bulk photovoltaic tensor β_{ilm}^L analysis**

81

82 Because our light source is linearly polarized, we only consider the linear BPV tensor β_{ilm}^L here. Without
 83 loss of generality, here we use a model structure, centrosymmetric orthorhombic unit cells with a strain
 84 gradient along x axis sketched in Supplementary Fig. 14, to represent the strain-gradient MoS₂ sheet in our
 85 study. As shown in Supplementary Fig. 14, the model structure includes symmetry elements of E, C₂(x),
 86 σ_v (xz) and σ_v (xy). Thus, the point group of this structure can be assigned to C_{2v}. The tensor β_{ilm}^L for C_{2v} is
 87 expressed as¹²

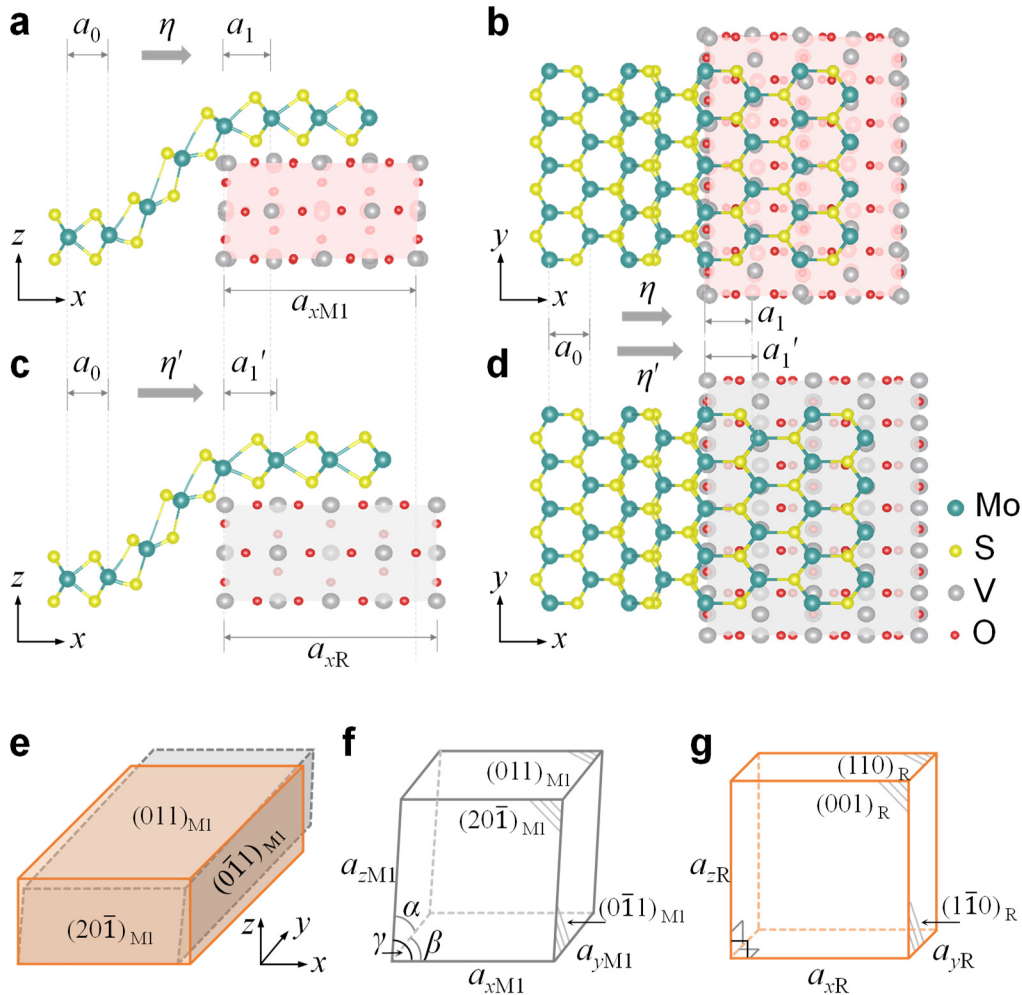
$$88 \quad \beta_{ilm}^L = \begin{bmatrix} 0 & 0 & \beta_{113} & 0 & 0 & 0 & \beta_{131} & 0 & 0 \\ 0 & 0 & 0 & 0 & 0 & \beta_{223} & 0 & \beta_{232} & 0 \\ \beta_{311} & 0 & 0 & 0 & \beta_{322} & 0 & 0 & 0 & \beta_{333} \end{bmatrix}, \quad (3)$$

89 where indexes 1, 2 and 3 correspond axes y , z , x , respectively. Since the laser path in our setup is
 90 perpendicular to the sample surface (along $-y$ axis), according to the Eq. (1) in the main text, the linearly
 91 polarized light-induced BPV current density j_i^L can be described as

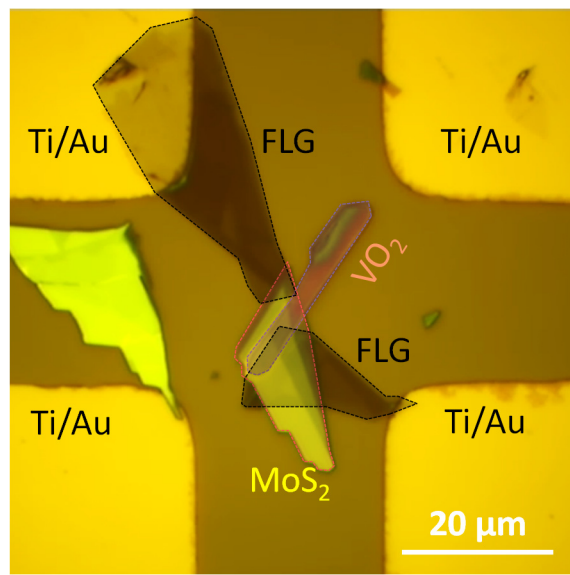
$$92 \quad j_i^L = \begin{pmatrix} (\beta_{113} + \beta_{131})\sin(\theta)\cos(\theta) \\ 0 \\ \beta_{311}\sin(\theta)^2 + \beta_{333}\cos(\theta)^2 \end{pmatrix} I, \quad (4)$$

93 where I is the light intensity and θ is the angle between the polarization direction of the light and the
 94 direction of the strain gradient (polar axis of the sample, x axis here). Due to the irregular geometry of
 95 contacts (inset of Fig. 2a in the main text), the current direction is not well defined. Thus, in our present
 96 study, the calculated values in the MoS₂ sheet represent effective values of β_{ilm}^L .

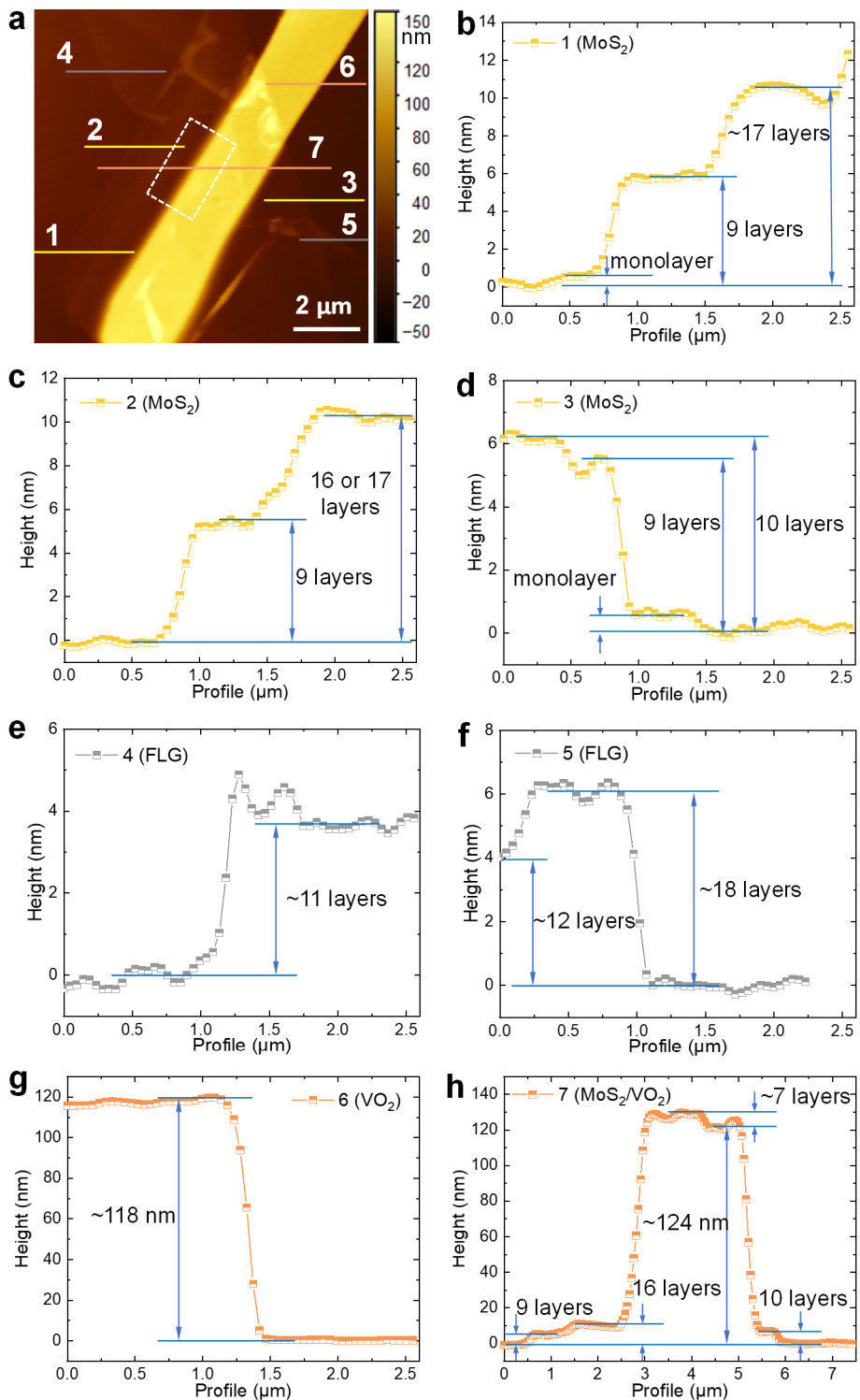
97 **Supplementary Figures**
 98



99
 100
 101 **Supplementary Fig. 1 | Schematics of strain gradient engineering in MoS₂.** **a,b**, Side view (**a**) and top view (**b**) of the hybrid system MoS₂/VO₂. The geometry of MoS₂ on the edge of VO₂ may induce a lattice change of MoS₂ (its lattice constant changes from a_0 to a_1), leading to a strain gradient η . Here monolayer structure of MoS₂ is chosen to illustrate the system clearly. **c,d**, Side view (**c**) and top view (**d**) of the hybrid system MoS₂/VO₂ after the structural phase transition of VO₂ from M1 phase to R phase (a change of lattice constant from $a_{x\text{M1}}$ to $a_{x\text{R}}$). The interaction between MoS₂ and VO₂ enables a change of the lattice constant of MoS₂ from a_1 to a_1' , leading to a modified strain gradient η' . Here, crystallographic orientations of MoS₂, x: [110], y: [110], z: [001]. **e–g**, Schematics of the shape (**e**) and supercells (**f** and **g**) of a VO₂ microbeam before (M1 phase, gray) and after (R phase, orange) the phase transition to demonstrate the lattice change. After the phase transition from M1 to R, the VO₂ lattice parameters along x and z directions have elongations of 0.3%, while the lattice parameter along y direction has a contraction of 0.9%.

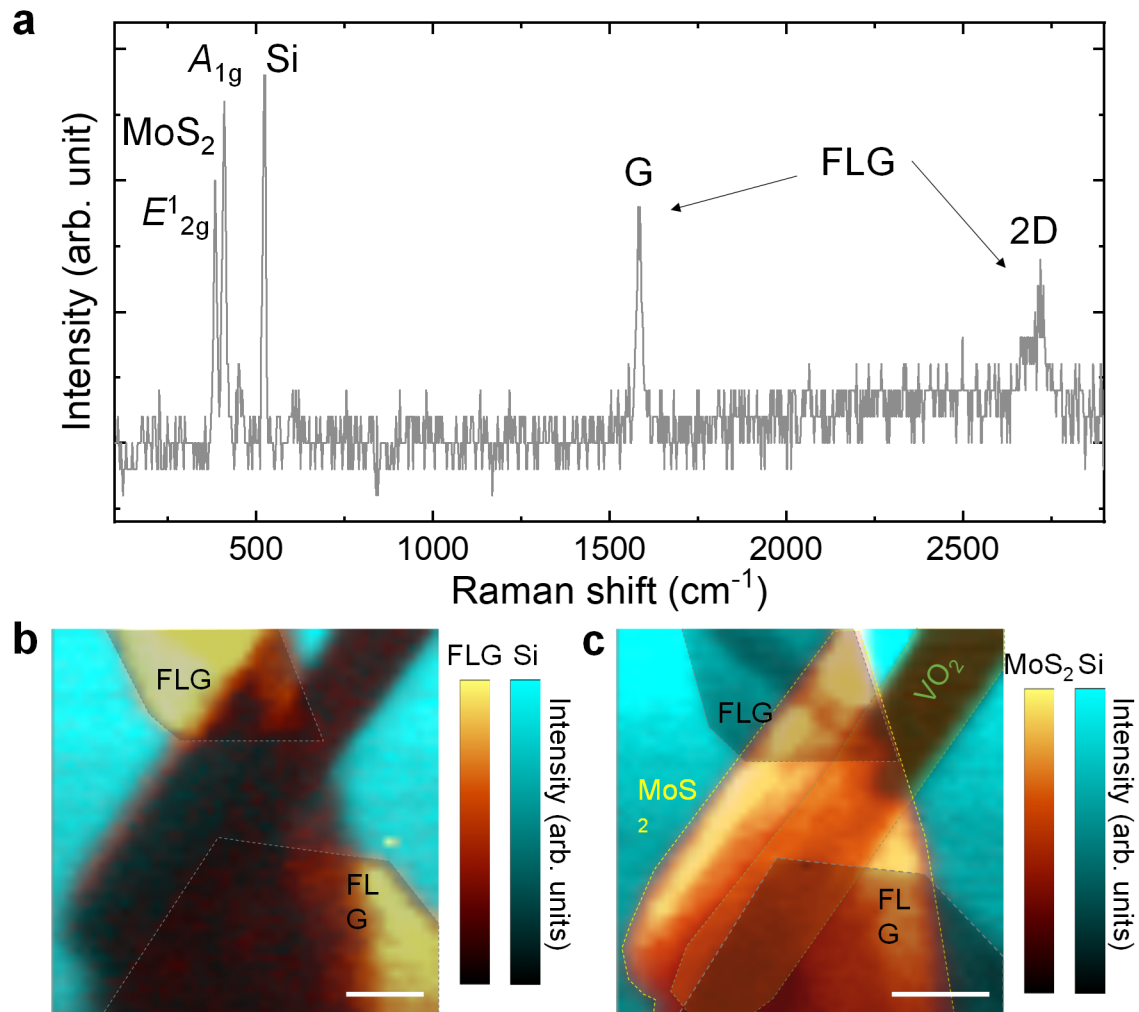


112
113
114 **Supplementary Fig. 2 | An optical image of a device consisting of an ultrathin MoS_2 sheet lying on a**
115 **VO_2 microbeam with two few-layer graphene (FLG) as contacts.**



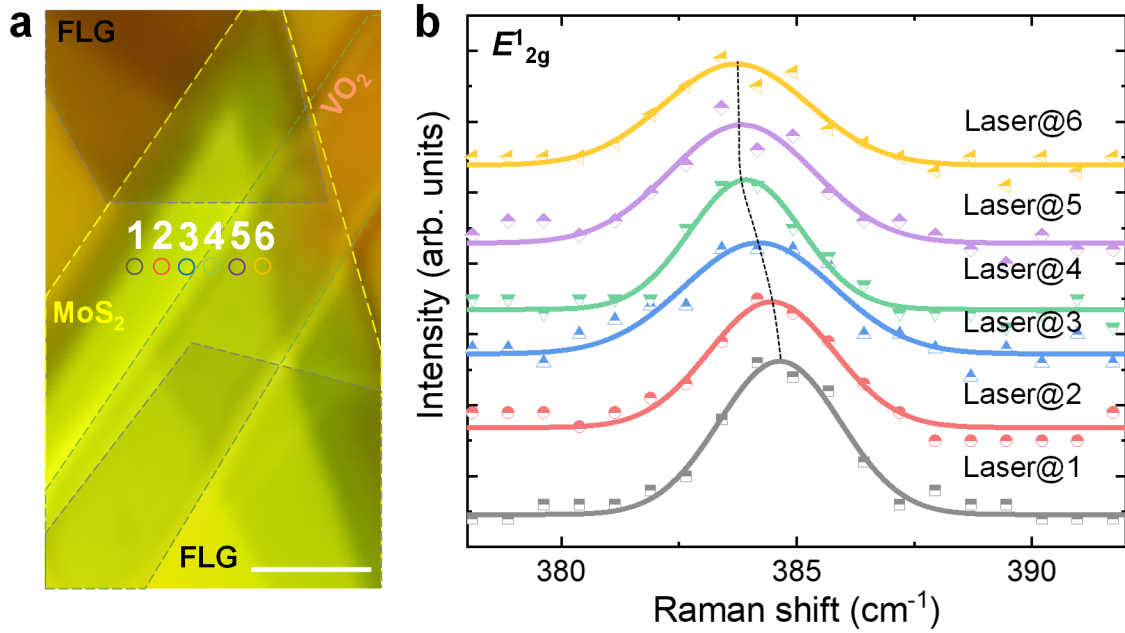
116
117

118 **Supplementary Fig. 3 | AFM measurements of the device.** **a–h**, AFM image (**a**), height profiles of yellow
119 lines 1 (**b**), 2 (**c**) and 3 (**d**) on the MoS₂ sheet, gray lines 4 (**e**) and 5 (**f**) on the FLG, orange line 6 (**g**) on the
120 VO₂ microbeam and line 7 (**h**) on the whole device. The regions of the MoS₂ sheet at the left edge, right
121 edge and surface of the VO₂ microbeam have about 16 (**c**), 10 (**d**) and 17 (**h**) layers, respectively. It is noted
122 that some layer numbers may not be accurate due to the uneven curves.

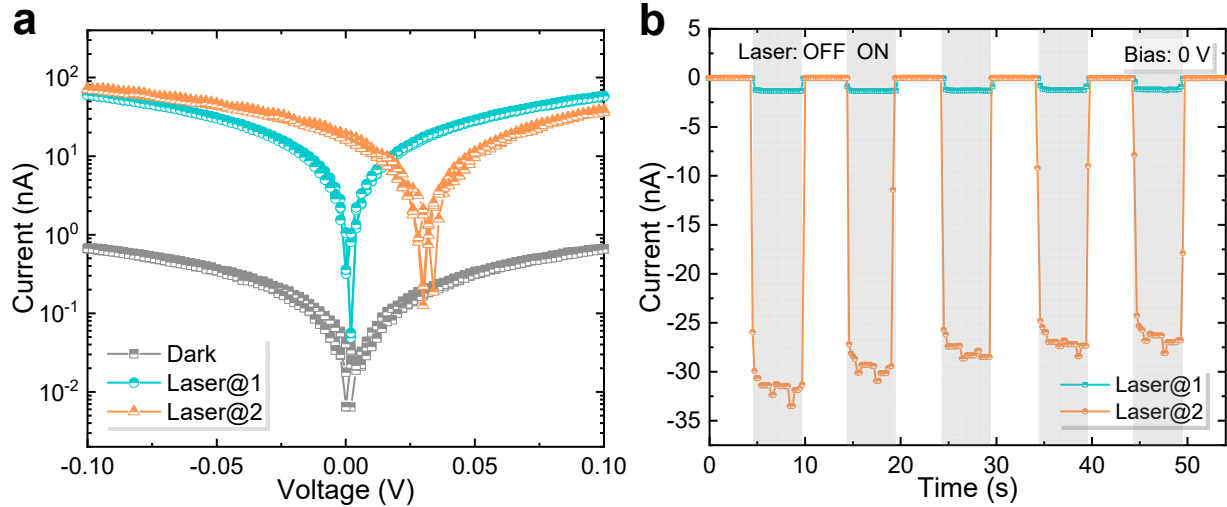


123
124
125
126
127
128
129

Supplementary Fig. 4 | Raman measurements of the MoS₂ sheet and FLG. **a**, A representative Raman spectrum measured at room temperature. E_{2g}^1 and A_{1g} modes of MoS₂¹³, G and 2D bands of FLG¹⁴ and Raman mode of Si¹⁵ were assigned. **b,c**, Raman mappings of FLG (**b**) and MoS₂ (**c**) at room temperature. Shapes of MoS₂, VO₂ and FLG are outlined by yellow, orange and gray dashed lines, respectively. Scale bars in **b** and **c**: 2 μ m.

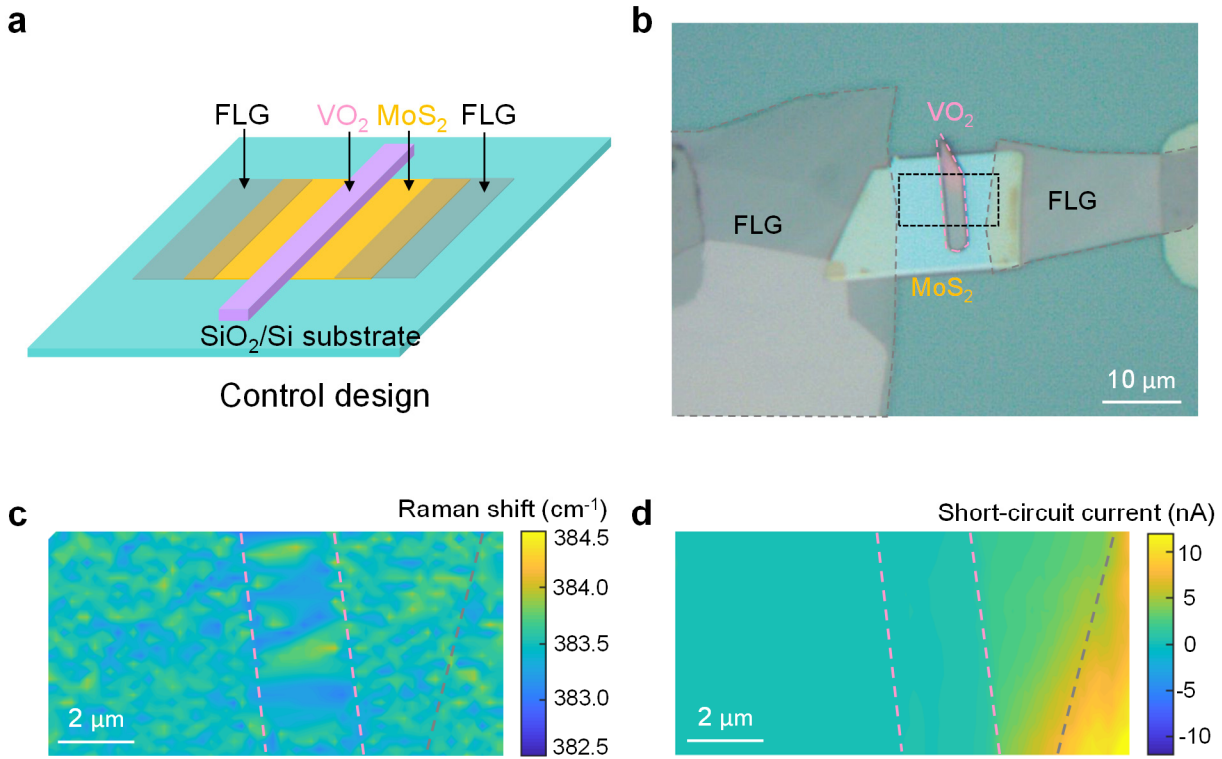


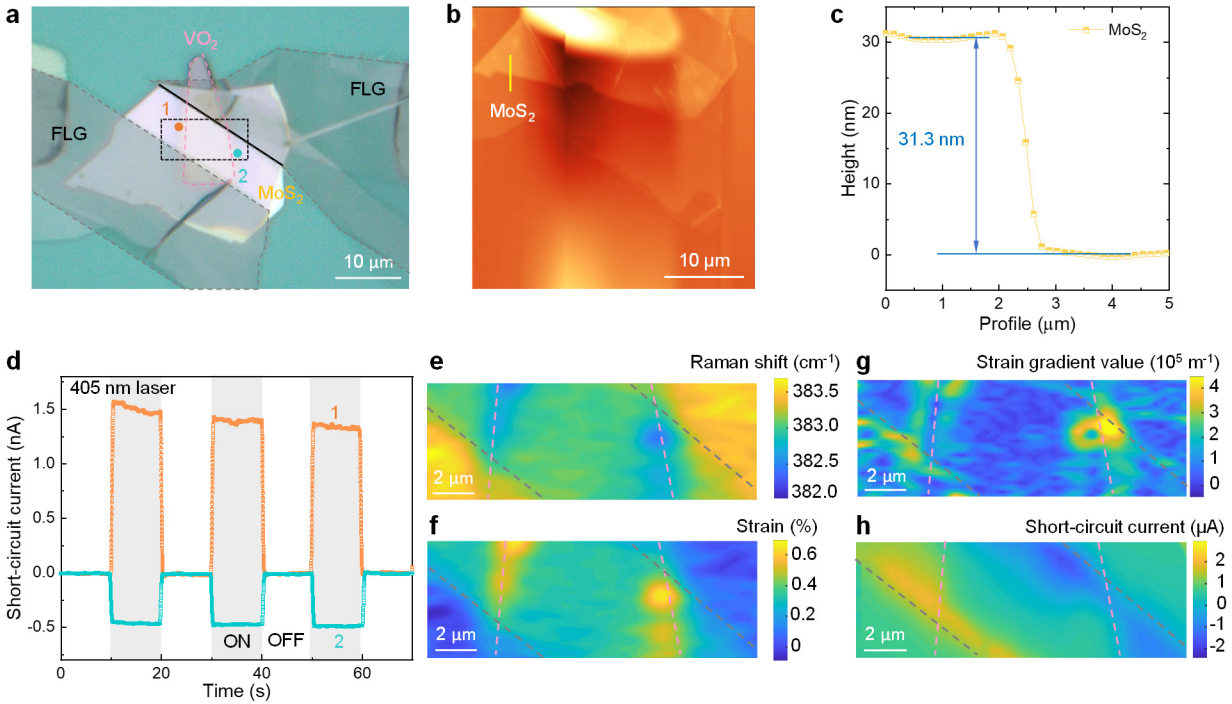
130
131
132 **Supplementary Fig. 5 | Raman spectra of E_{2g}^1 mode of MoS_2 (b) measured at laser spots 1–6 shown in**
133 **an optical image of the device (a).** Raman spectra of the MoS_2 sheet for laser spots 4–6 on the VO_2
134 **microbeam show a red shift of E_{2g}^1 mode, indicating a tensile strain in the region of the MoS_2 sheet on the**
135 **microbeam and a strain gradient in the region at the edge of the microbeam. Black dashed line in b is a**
136 **guide for the eye. Shapes of the MoS_2 , VO_2 and FLG are outlined by yellow, orange and gray dashed lines,**
137 **respectively. Scale bar in a: 2 μm .**



138
139

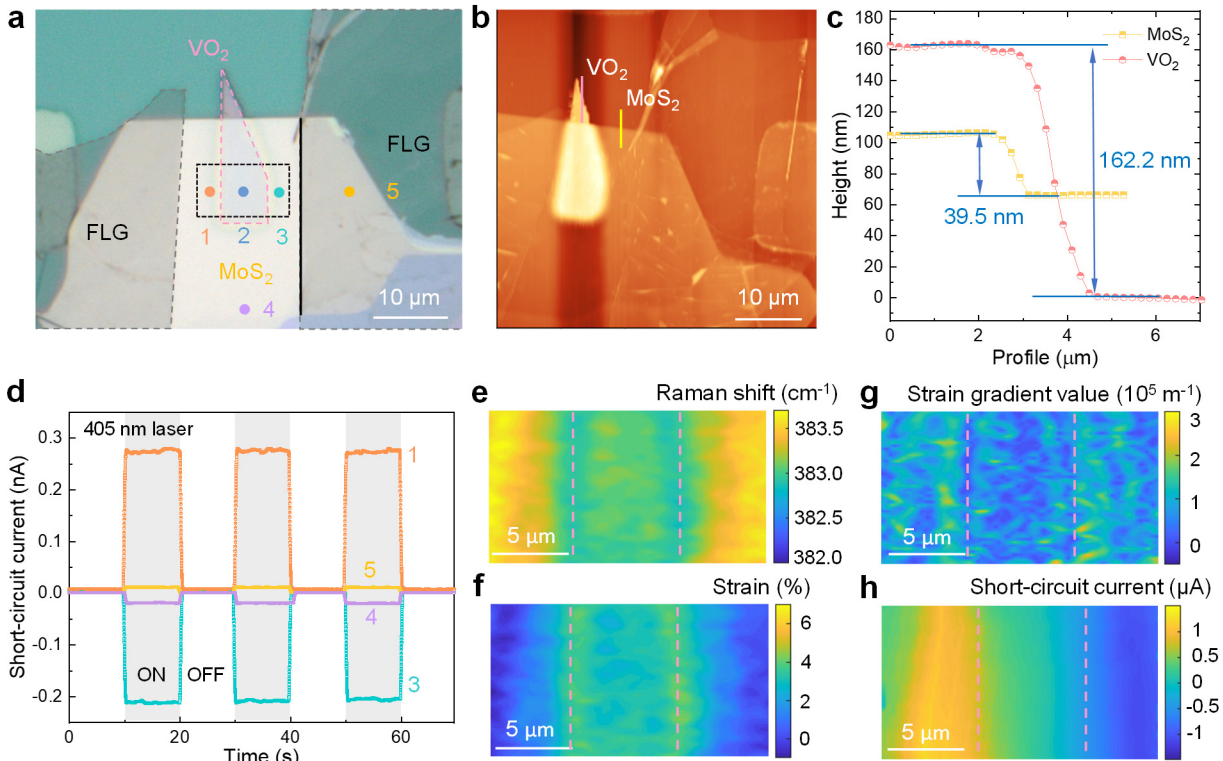
140 **Supplementary Fig. 6 | Photocurrent measurements of the MoS₂ sheet under laser (532 nm)**
 141 **illumination at different positions.** **a**, Current in a logarithmic scale versus voltage curves under laser
 142 illumination at the region with a small strain gradient (Laser@1, spot 1 in insets of Fig. 2a,e in the main
 143 text) and with a large strain gradient (Laser@2, spot 2 in insets of Fig. 2a,e in the main text) and current-
 144 voltage curve without laser illumination (Dark) for comparison. **b**, Photo response with laser illumination
 145 “ON” (light gray shadow) and “OFF” at spots 1 (Laser@1) and 2 (Laser@2) with zero bias voltage. The
 146 photocurrent for spot 2 (~30 nA) is about 23 times of that for spot 1 (~1.3 nA).

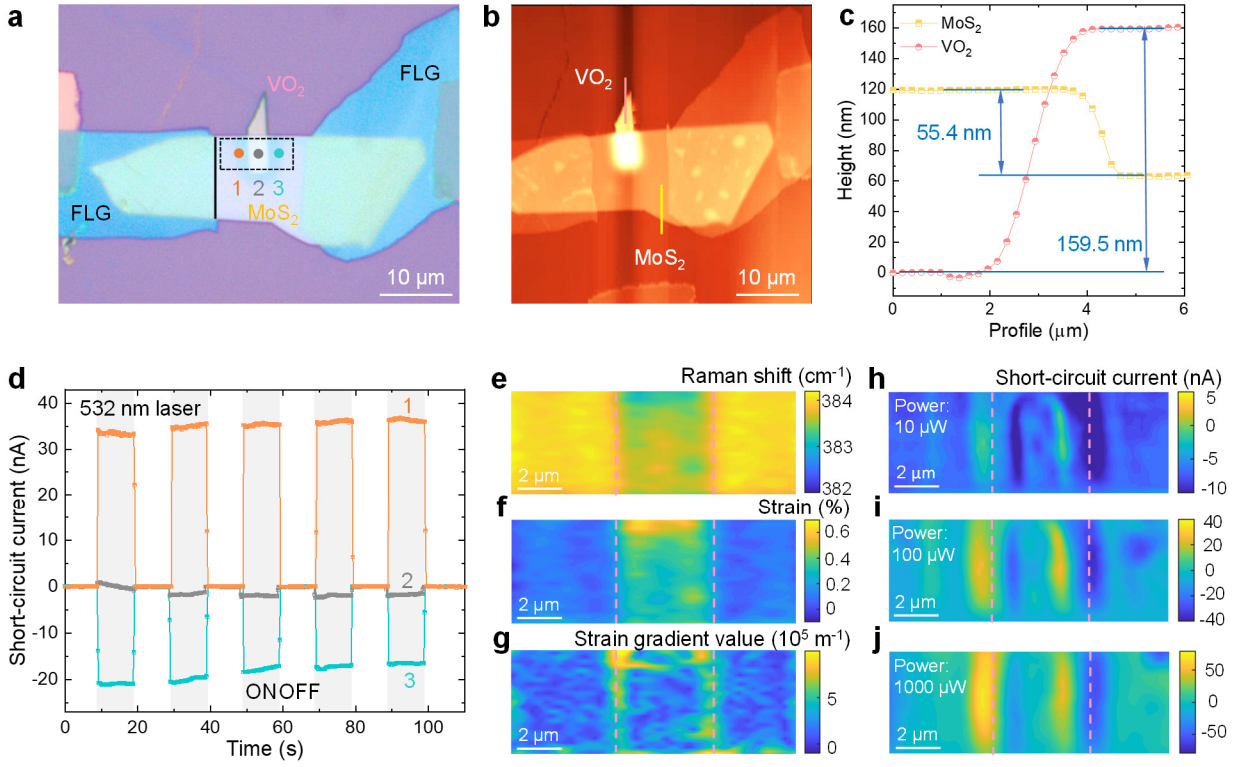




159
160

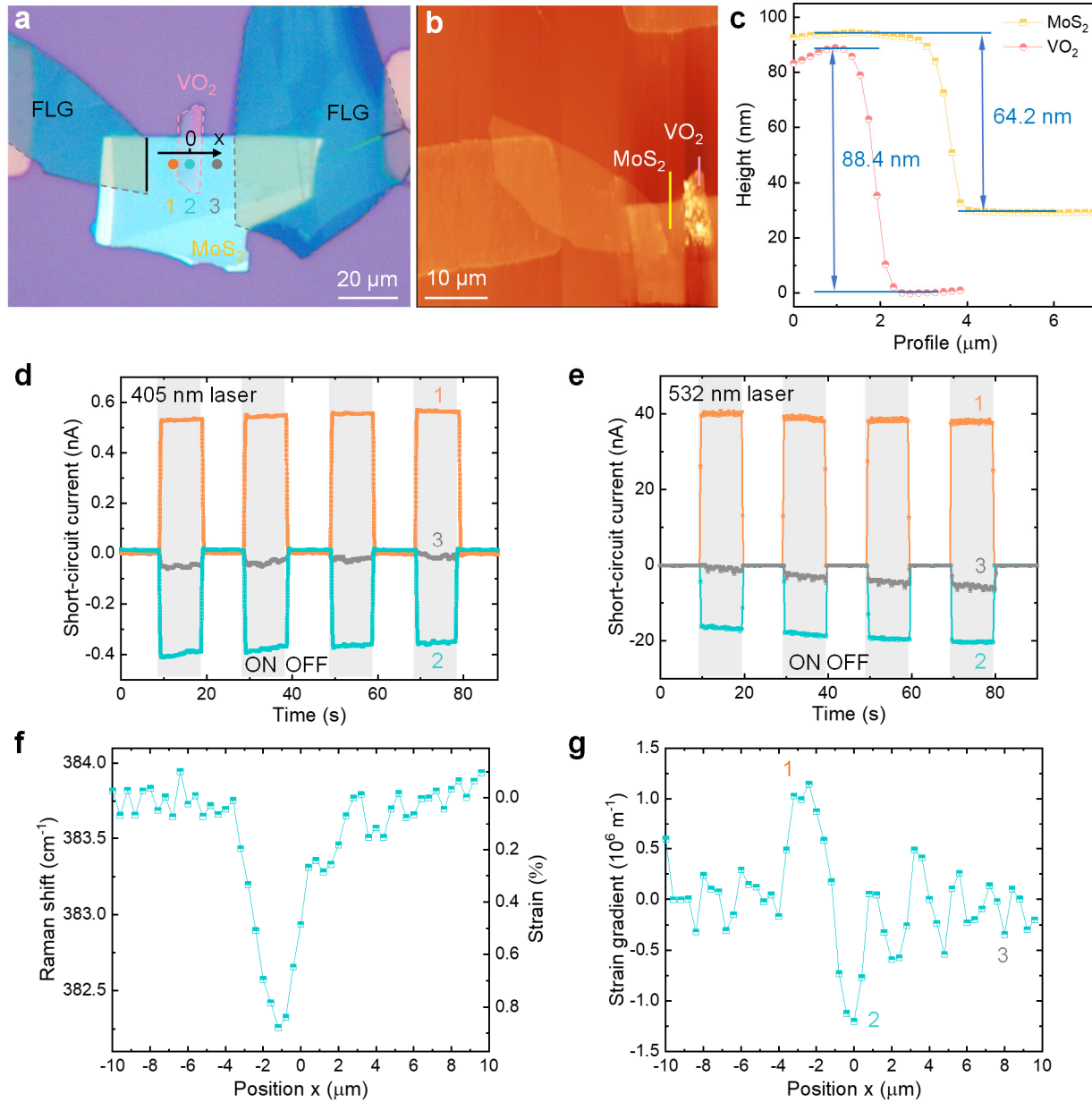
161 **Supplementary Fig. 8 | FPV effect of the MoS_2 sheet in device #2 at room temperature.** **a**, Optical
162 image of device #2. The length of the contact between the MoS_2 and FLG (black solid line) is estimated to
163 be $22.4 \mu\text{m}$. **b**, AFM image of the device. **c**, Height profile of the yellow line (MoS_2) in **b**. The thickness of
164 the MoS_2 is estimated to be 31.3 nm . **d**, Photo responses with laser (405 nm) illumination “ON” (light gray
165 shadow) and “OFF” at spots 1 (orange dot in **a**) and 2 (cyan dot in **a**) with zero bias voltage. **e**, Raman
166 mapping of E_{2g}^1 mode of MoS_2 on the device. **f**, Strain map of the MoS_2 sheet calculated from **e**. **g**, Map of
167 strain gradient value in the MoS_2 sheet calculated from **f**. **h**, Short-circuit photocurrent map of the device
168 measured under illumination by a 532 nm laser. The mapping area is outlined in the black dashed rectangle
169 in **a**. Shapes/boundaries of the VO_2 microbeam and FLGs are outlined in pink and gray dashed lines,
170 respectively, in **a** and **e-h**.





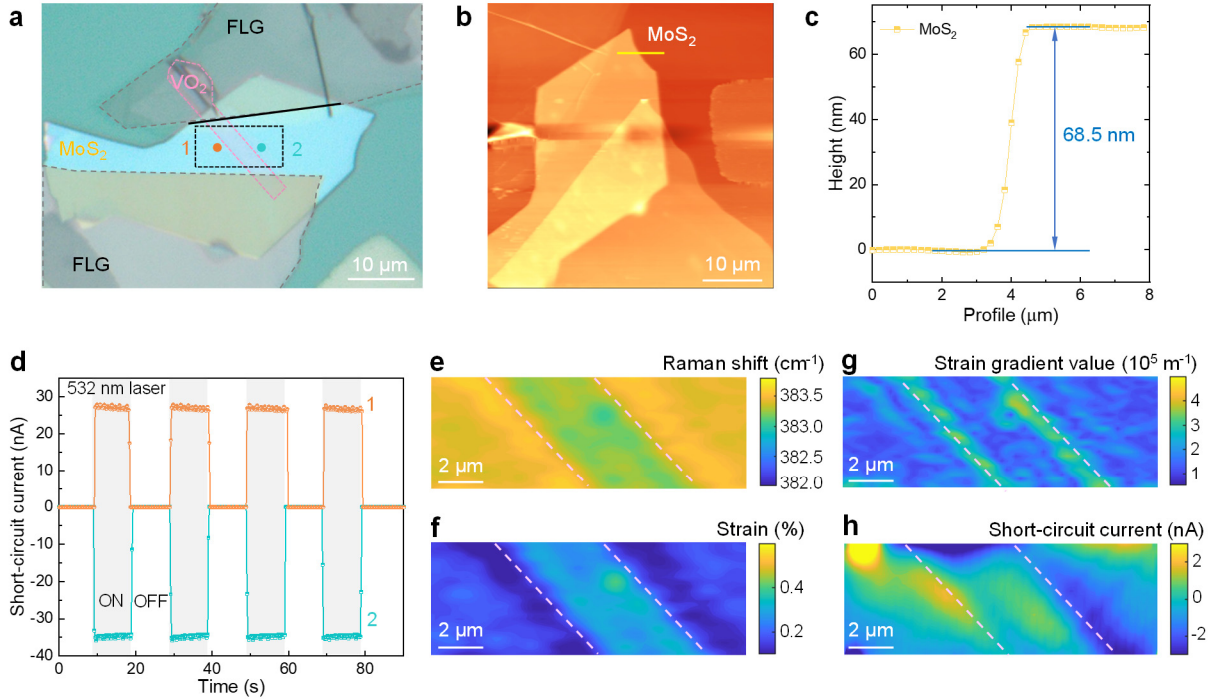
184
185

186 **Supplementary Fig. 10 | FPV effect of the MoS₂ sheet in device #4 at room temperature.** **a**, Optical
187 image of device #4. The length of the contact between the MoS₂ and FLG (black solid line) is estimated to
188 be 13.9 μm. **b**, AFM image of the device. **c**, Height profiles of the yellow line (MoS₂) and pink line (VO₂)
189 in **b**. The thicknesses of the MoS₂ sheet and VO₂ microbeam are estimated to be 55.4 nm and 159.5 nm,
190 respectively. **d**, Photo responses with laser (532 nm) illumination “ON” (light gray shadow) and “OFF” at
191 spots 1, 2 and 3 (orange, gray and cyan dots in **a**, respectively) with zero bias voltage. **e**, Raman mapping
192 of E_{2g}^1 mode of MoS₂ on the device. **f**, Strain map of the MoS₂ sheet calculated from **e**. **g**, Map of strain
193 gradient value in the MoS₂ sheet calculated from **f**. **h–j**, Short-circuit photocurrent maps of the device
194 measured under illumination by a 532 nm laser. The laser power of 10 μW, 100 μW and 1000 μW are used
195 in **h**, **i** and **j**, respectively. The mapping area is outlined in the black dashed rectangle in **a**. Both edges of
196 the VO₂ microbeam are outlined in pink dashed lines in **e–j**.



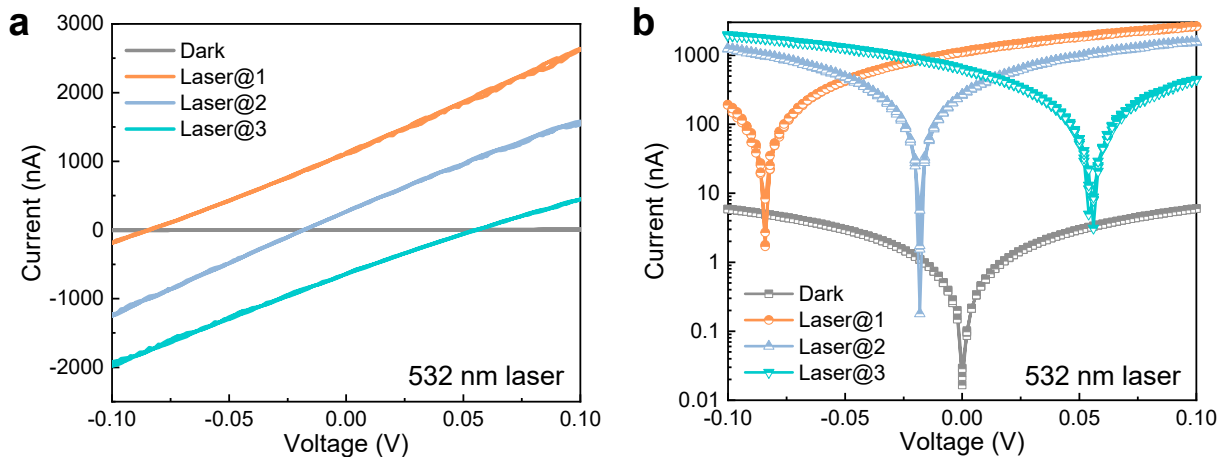
199
200
201
202
203
204
205
206
207
208
209

Supplementary Fig. 11 | FPV effect of the MoS_2 sheet in device #5 at room temperature. **a**, Optical image of device #5. The length of the contact between the MoS_2 and FLG (black solid line) is estimated to be 18.1 μm . Shapes of the VO_2 microbeam and FLGs are outlined in pink and gray dashed lines, respectively. **b**, AFM image of the device. **c**, Height profiles of the yellow line (MoS_2) and pink line (VO_2) in **b**. The thicknesses of the MoS_2 sheet and VO_2 microbeam are estimated to be 64.2 nm and 88.4 nm, respectively. **d,e**, Photo responses with laser (405 nm in **d** and 532 nm in **e**) illumination “ON” (light gray shadow) and “OFF” at spots 1, 2 and 3 (orange, cyan and gray dots in **a**, respectively) with zero bias voltage. **f**, Raman line scan of E_{2g}^1 mode of MoS_2 on the device (left axis) and corresponding strains in the MoS_2 sheet (right axis). The scanning line is shown as the black arrow in **a**. **g**, Strain gradient values in the MoS_2 sheet calculated from **f**. Spots 1, 2 and 3 correspond to positions around the maximum, minimum and zero values of strain gradients.



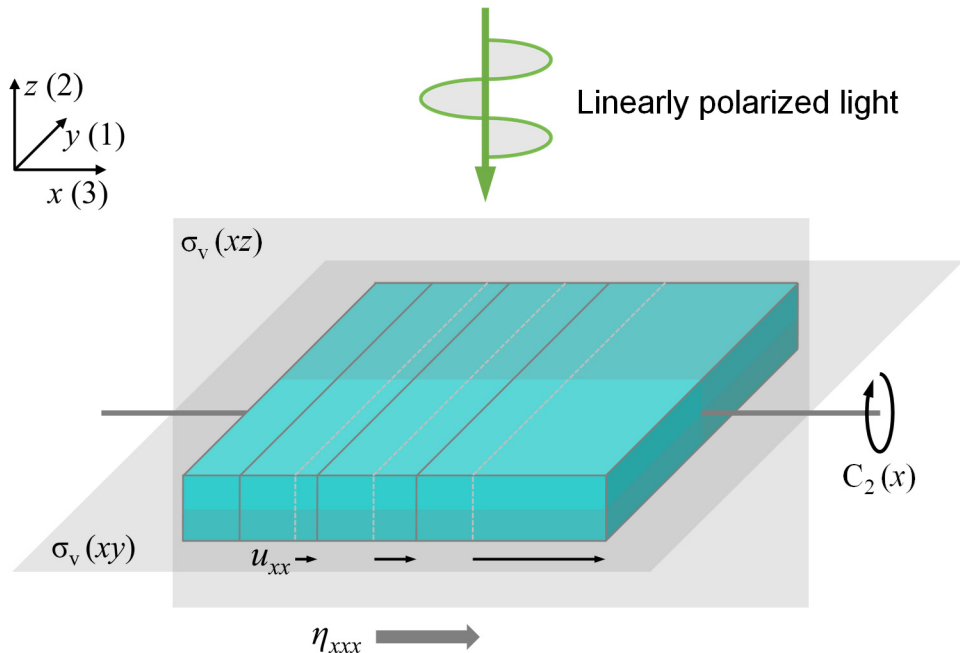
210
211
212
213
214
215
216
217
218
219
220
221

Supplementary Fig. 12 | FPV effect of the MoS₂ sheet in device #6 at room temperature. **a**, Optical image of device #6. The length of the contact between the MoS₂ and FLG (black solid line) is estimated to be 21.1 μm . **b**, AFM image of the device. **c**, Height profile of the yellow line (MoS₂) in **b**. The thickness of the MoS₂ sheet is estimated to be 68.5 nm. **d**, Photo responses with laser (532 nm) illumination “ON” (light gray shadow) and “OFF” at spots 1 and 2 (orange and cyan dots in **a**, respectively) with zero bias voltage. **e**, Raman mapping of E_{2g}^1 mode of MoS₂ on the device. **f**, Strain map of the MoS₂ sheet calculated from **e**. **g**, Map of strain gradient value in the MoS₂ sheet calculated from **f**. **h**, Short-circuit photocurrent map of the device measured under illumination by a 532 nm laser. The mapping area is outlined in the black dashed rectangle in **a**. Shapes/boundaries of the VO₂ microbeam and FLGs are outlined in pink and gray dashed lines, respectively in **a** and **e–h**.



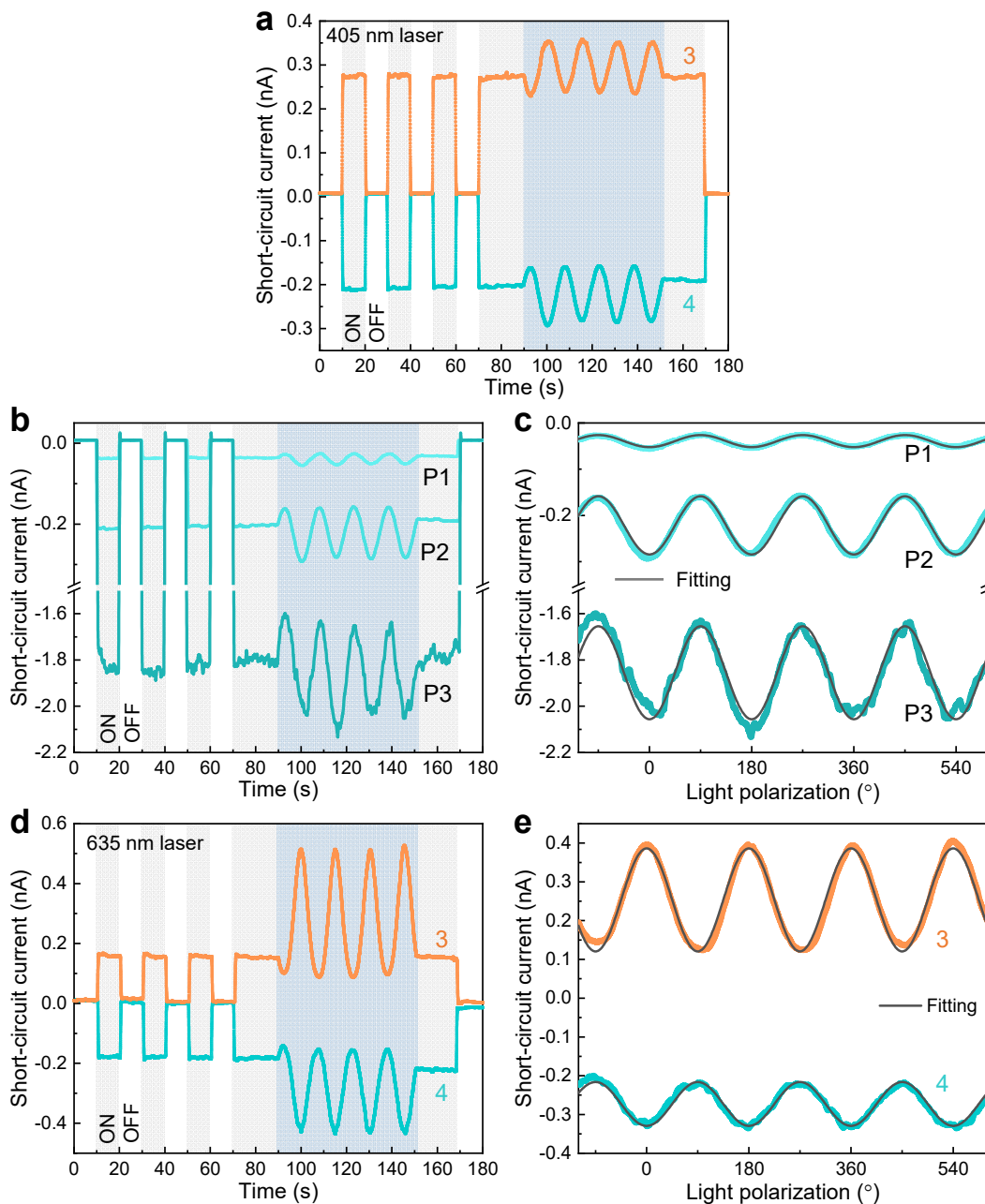
222
223
224
225
226
227

Supplementary Fig. 13 | Current-voltage characterizations of the MoS₂ sheet in device #3 under laser (532 nm) illumination at spots 1, 2 and 3 (Laser@1, Laser@2 and Laser@3) and without illumination (Dark) for comparison. a, Linear plots. b, Logarithmic plots. The spots 1, 2 and 3 are outlined in orange, blue and cyan, respectively, in Supplementary Fig. 9a.



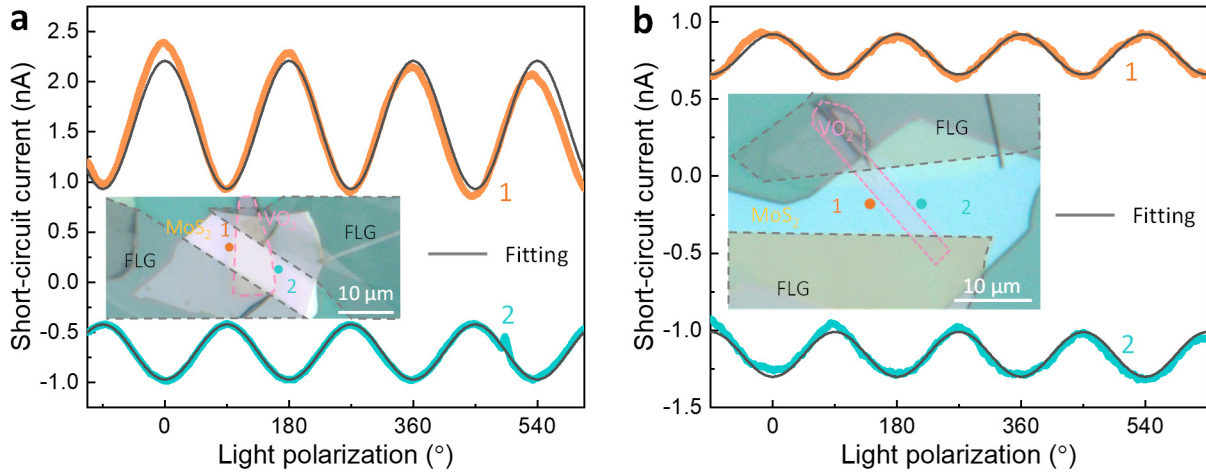
228
229

230 **Supplementary Fig. 14 | A model structure consisting centrosymmetric orthorhombic unit cells with**
231 **a strain gradient η_{xxx} along x axis (strain u_{xx} varies).** The crystal has symmetry elements of E, $C_2(x)$,
232 $\sigma_v(xz)$ and $\sigma_v(xy)$, thus its point group can be assigned to C_{2v} .



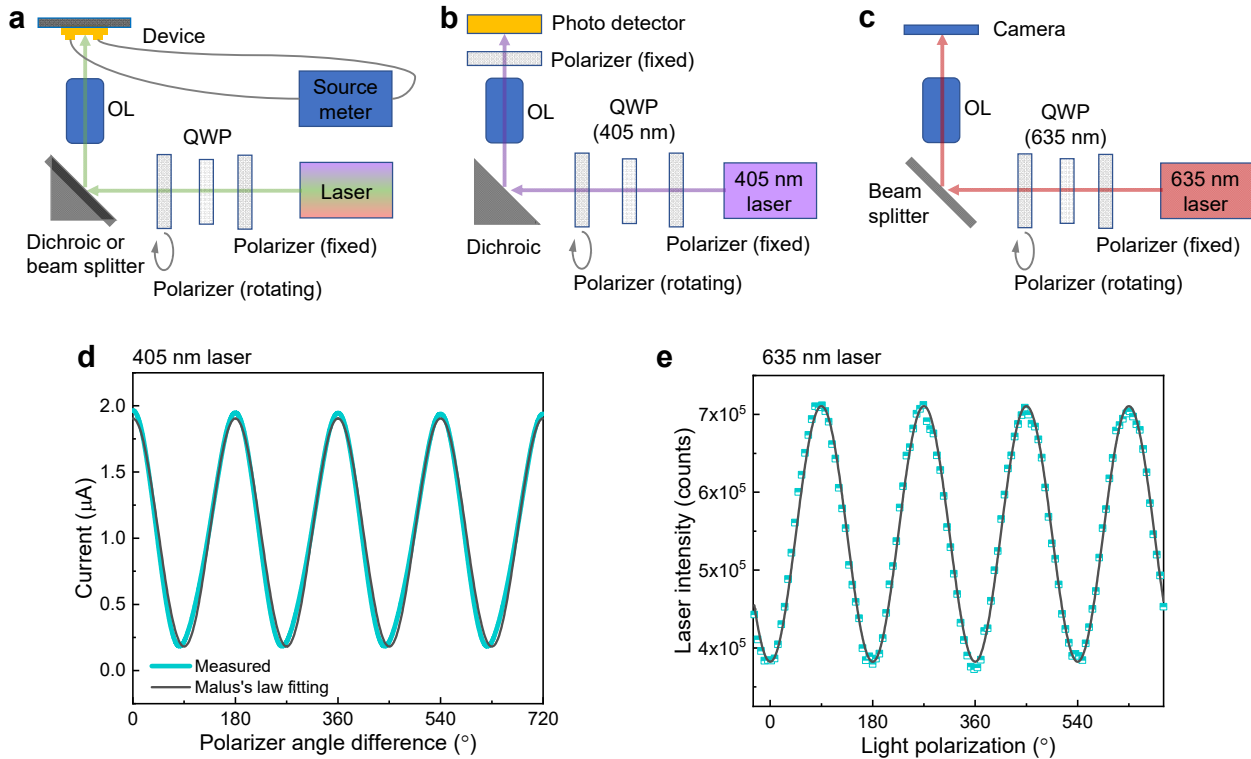
233
234

235 **Supplementary Fig. 15 | Light polarization dependence of the short-circuit photocurrent in device #3**
236 **at room temperature.** **a**, Short-circuit photocurrent responses under laser (405 nm) illumination “ON”
237 (light gray shadow) and “OFF” at spot 3 and 4 (inset of Fig. 2g in the main text) and their light polarization
238 dependence (light blue region). **b**, Laser power dependence of photocurrent measurements. P1, P2 and P3
239 represent powers of 3.8 nW, 39.1 nW and 389 nW, respectively. **c**, Photocurrents as a function of light (405
240 nm) polarization and fittings (gray curves). Fittings yield β_{333} of $6.3 \times 10^{-3} \text{ V}^{-1}$, $6.5 \times 10^{-3} \text{ V}^{-1}$ and $1.9 \times 10^{-2} \text{ V}^{-1}$,
241 and β_{311} of $3.2 \times 10^{-3} \text{ V}^{-1}$, $3.6 \times 10^{-3} \text{ V}^{-1}$ and $1.5 \times 10^{-2} \text{ V}^{-1}$ for P1, P2 and P3, respectively. **d**, Same
242 measurements as those in **a** under illumination with a 635 nm laser. **e**, Calibrated photocurrents as a function
243 of light (635 nm) polarization and fittings (gray curves). Fittings yield β_{333} of $1.2 \times 10^{-2} \text{ V}^{-1}$ and $1.2 \times 10^{-2} \text{ V}^{-1}$,
244 and β_{311} of $7.8 \times 10^{-3} \text{ V}^{-1}$ and $4.3 \times 10^{-3} \text{ V}^{-1}$ for the upper curve and lower curve, respectively.



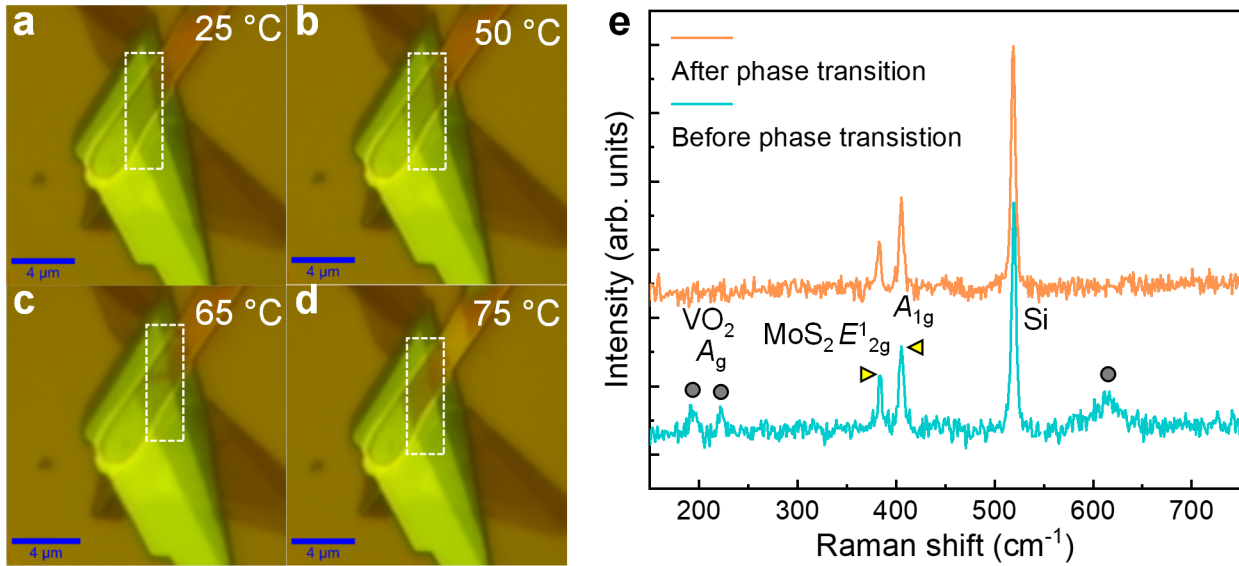
245
246
247
248
249
250
251
252
253
254

Supplementary Fig. 16 | Light polarization dependence of the short-circuit photocurrent in devices #2 (a) and #6 (b) at room temperature. Insets of **a** and **b** are optical images of devices #2 and #6, respectively. The MoS₂ sheets, VO₂ microbeams and FLGs are outlined in yellow, pink and gray dashed lines, respectively. A 405 nm laser with power densities of 6.32 W cm^{-2} and 227.9 W cm^{-2} is used for measurements on devices #2 and #6, respectively. Fittings (gray curves) in **a** (device #2) yield β_{333} of $5.0 \times 10^{-2} \text{ V}^{-1}$ and $2.2 \times 10^{-2} \text{ V}^{-1}$, and β_{311} of $2.1 \times 10^{-2} \text{ V}^{-1}$ and $9.5 \times 10^{-3} \text{ V}^{-1}$ for the upper curve and lower curve, respectively. Fittings (gray curves) in **b** (device #6) yield β_{333} of $3.9 \times 10^{-4} \text{ V}^{-1}$ and $2.8 \times 10^{-4} \text{ V}^{-1}$, and β_{311} of $3.1 \times 10^{-4} \text{ V}^{-1}$ and $2.0 \times 10^{-4} \text{ V}^{-1}$ for the upper curve and lower curve, respectively.



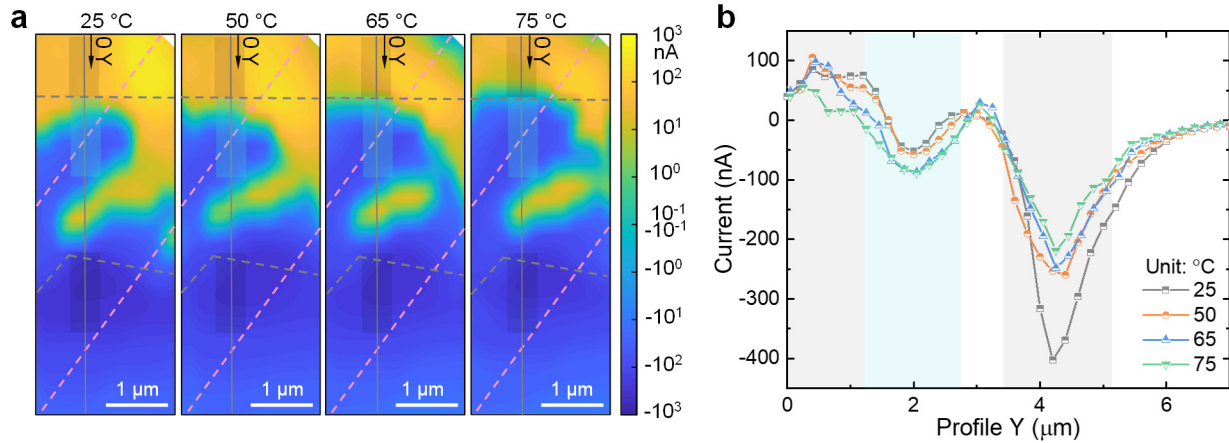
255
256
257
258
259
260
261
262
263
264
265
266

Supplementary Fig. 17 | Calibration of optical setup. **a**, Schematic of the setup for the light polarization dependence measurement. The optical elements in the path from the laser to the device include fixed polarizer, quarter wave plate (QWP), rotating polarizer, dichroic or beam splitter and objective lens (OL). **b**, Schematic of the setup for calibrating the 405 nm laser after the optical elements. **c**, Schematic of the setup for calibrating the 635 nm laser after the optical elements. **d**, Photocurrent of the detector as function of angle difference between two polarizers for the case of **b**. The measured data is well fitted to Malus's law ($I = I_0 \cos^2 \theta$, where I is the light intensity arrived on the photodetector and it is proportional to the photocurrent), indicating that the intensity of the polarized light after the optical elements in **a** is nearly constant with rotating the polarizer. **e**, Laser intensity as a function of light polarization for the case of **c**. Our measured photocurrent is normalized with the measured light intensity in **e**.



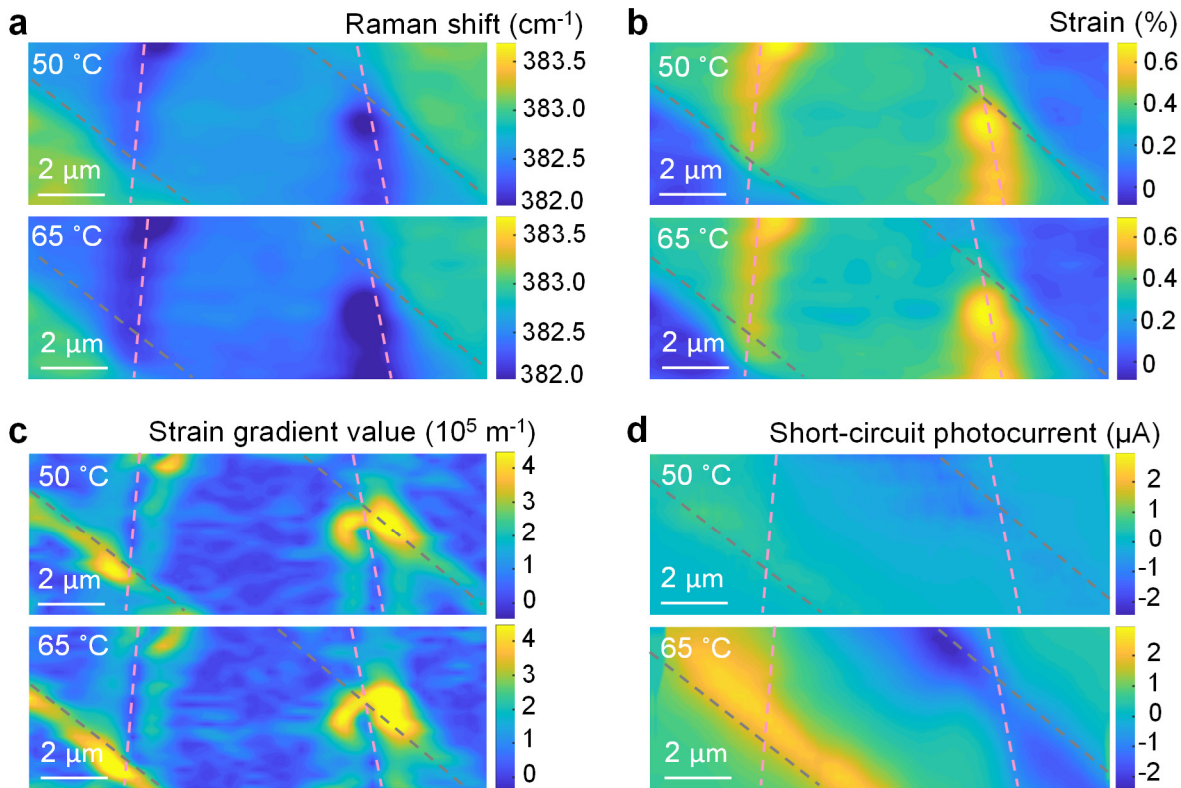
267
268
269
270
271
272
273
274

Supplementary Fig. 18 | Structural phase transition of the VO₂ microbeam. **a–d**, Optical images of the device at 25 °C (**a**), 50 °C (**b**), 65 °C (**c**) and 75 °C (**d**). The contrast changes at 65 °C (small domain) and 75 °C (large domain) indicate that the structural phase transition of the VO₂ microbeam emerges at 65 °C. **e**, Raman spectra of the MoS₂ sheet on the microbeam before (cyan) and after (orange) the phase transition of the microbeam. A_g modes (circles) of VO₂ in the cyan spectrum disappear in the orange spectrum, confirming the phase transition of the microbeam from M1 to R phase.



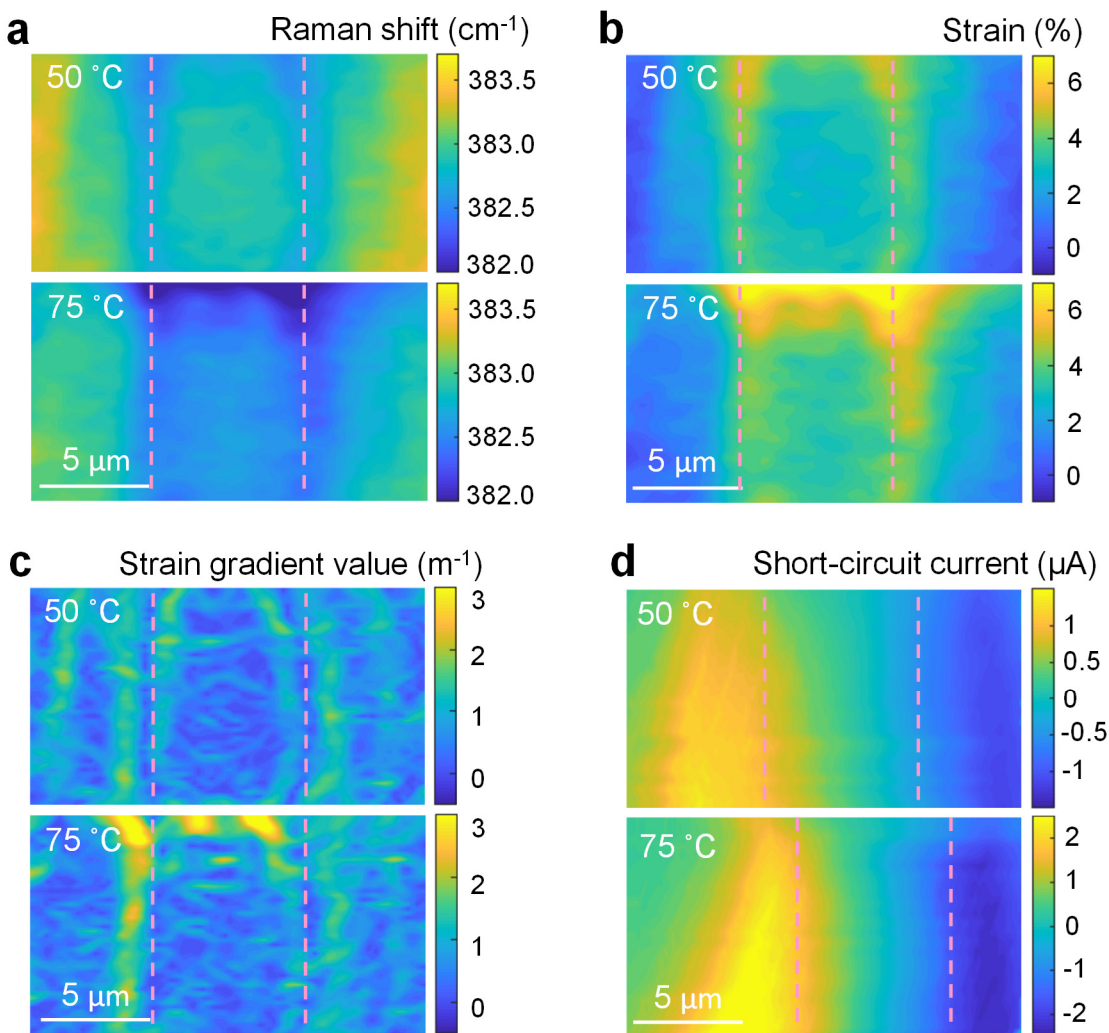
275
276
277
278
279
280
281

Supplementary Fig. 19 | Temperature-dependent short-circuit photocurrent maps (a) and profiles (b). **a**, Short-circuit photocurrent maps of device #1 at 25–75 °C. **b**, Short-circuit photocurrent profiles Y extracted from the gray lines in **a** at 25–75 °C. The light cyan region corresponds to the region on an edge of the VO₂ microbeam. Light gray regions in **a** along profiles Y correspond to the contact regions with small strain gradients.



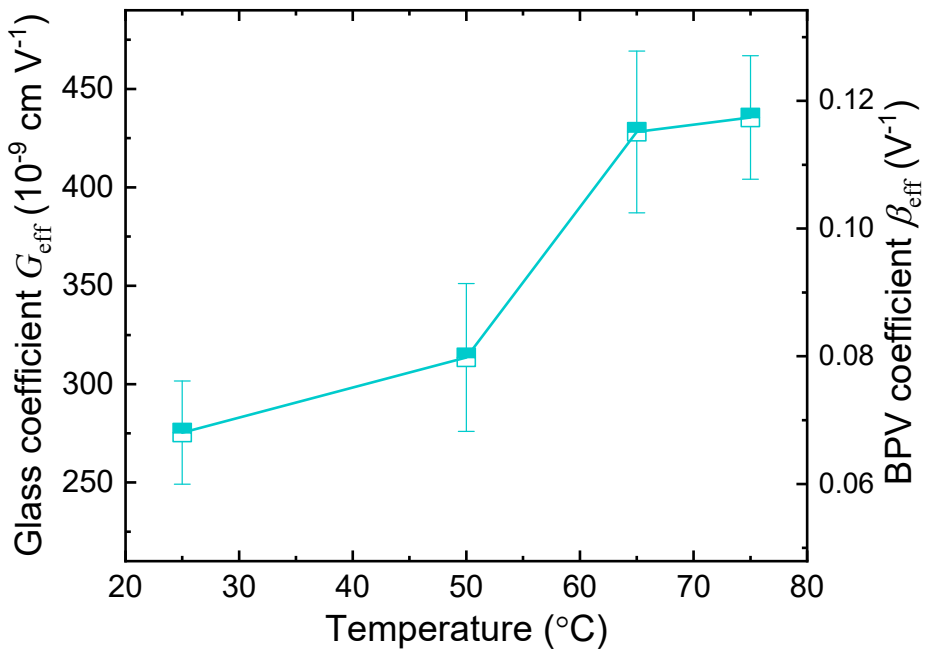
282
283
284
285
286
287
288
289
290

Supplementary Fig. 20 | FPV effect of the MoS₂ sheet in device #2 at 50 °C and 65 °C (before and after phase transition of the VO₂ microbeam). **a**, Raman mapping of E_{2g}^1 mode of MoS₂ on the device at 50 °C and 65 °C. **b**, Strain maps of the MoS₂ sheet at 50 °C and 65 °C calculated from **a**. **c**, Maps of strain gradient value of the MoS₂ sheet at 50 °C and 65 °C calculated from **b**. **d**, Short-circuit photocurrent maps of the device at 50 °C and 65 °C. The mapping area is outlined in the black dashed rectangle in Supplementary Fig. 8a. Boundaries of the VO₂ microbeam and FLG are outlined in pink and gray dashed lines, respectively.



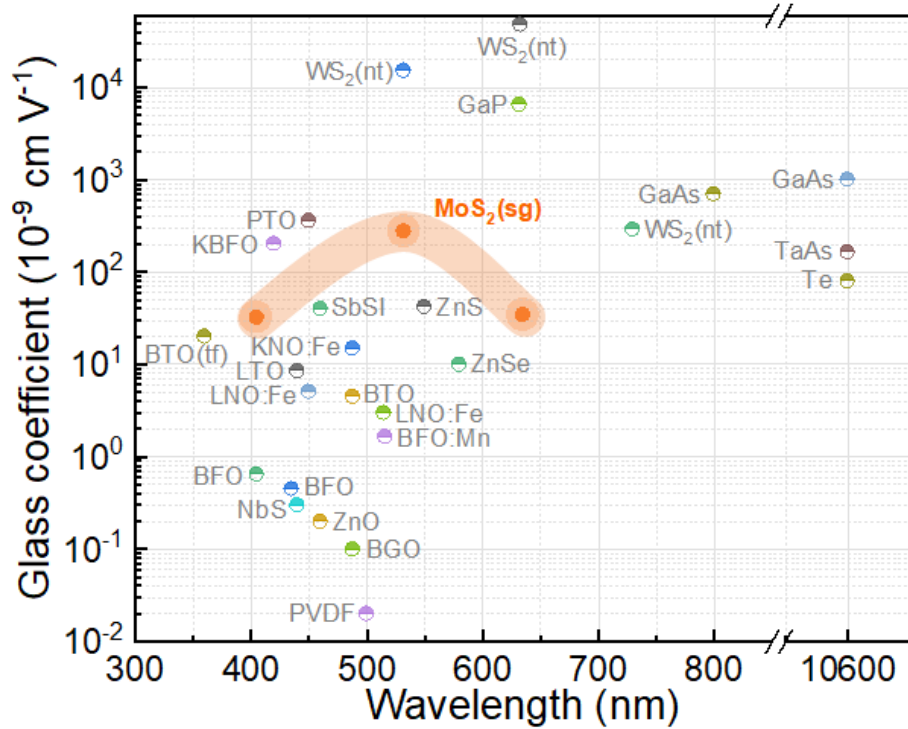
291
292

293 **Supplementary Fig. 21 | FPV effect of the MoS₂ sheet in device #3 at 50 °C and 75 °C (before and**
294 **after phase transition of the VO₂ microbeam).** **a**, Raman mapping of E_{2g}^1 mode of MoS₂ on the device at
295 50 °C and 75 °C. **b**, Strain maps of the MoS₂ sheet at 50 °C and 75 °C calculated from **a**. **c**, Maps of strain
296 gradient value of the MoS₂ sheet at 50 °C and 75 °C calculated from **b**. **d**, Short-circuit photocurrent maps
297 of the device at 50 °C and 65 °C. The mapping area is outlined in the black dashed rectangle in
298 Supplementary Fig. 9a. Boundaries of the VO₂ microbeam are outlined in pink dashed lines.



299
300
301
302

Supplementary Fig. 22 | Temperature-dependent maximum Glass coefficient G_{eff} and BPV coefficient β_{eff} obtained from Fig. 3g in the main text.



303
304
305 **Supplementary Fig. 23 | An overview of Glass coefficients in reported materials.** The effective Glass
306 coefficients in $\text{MoS}_2(\text{sg})$ calculated in the present study are shown in orange circles highlighted by the light
307 orange shadow. Our data points at the wavelength of 405 nm, 532 nm and 635 nm are obtained from devices
308 #2, #1 and #3 at room temperature, respectively. Data for other materials are taken from the literature: WS_2
309 nanotube (nt)¹⁶, GaP ¹⁷, GaAs ¹², PbTiO_3 ¹², KBiFe_2O_5 (KBFO)¹⁸, TaAs ¹⁹, Te ¹², SbSI ²⁰, ZnS ¹², BaTiO_3 thin
310 film (BTO(tf))²¹, KNO:Fe ¹², ZnSe ¹², LiTaO_3 (LTO)¹², Fe-doped LiNbO_3 (LNO:Fe)^{22,23}, BTO¹², Mn-doped
311 BiFeO_3 (BFO:Mn)²⁴, BiFeO_3 (BFO)²⁵, NbS ¹², ZnO ²⁶, $\text{Bi}_{12}\text{GeO}_{20}$ (BGO)²⁷ and polyvinylidene fluoride
312 (PVDF)¹². Data for SbSI, BTO(tf), LTO, BTO, BFO:Mn, BFO (light blue) and ZnO are G_{31} , for Te and
313 LNO:Fe are G_{33} , for BFO (orange) is G_{22} , for BGO is G_{14} , and for others are effective values. All data are
314 for linear BPV effect.

315 **References**

- 316
- 317 1. Belinicher, V., Ivchenko, E. & Sturman, B. Kinetic theory of the displacement photovoltaic effect in
318 piezoelectrics. *Zh Eksp Teor Fiz* **83**, 649-661 (1982).
- 319 2. Sturman, B. I. Ballistic and shift currents in the bulk photovoltaic effect theory. *Physics-Uspekhi* **63**,
320 407-411 (2020).
- 321 3. Nagaosa, N. & Morimoto, T. Concept of quantum geometry in optoelectronic processes in solids:
322 Application to solar cells. *Adv. Mater.* **29**, 1603345 (2017).
- 323 4. Král, P. Quantum kinetic theory of shift-current electron pumping in semiconductors. *J. Phys.: Condens.
324 Matter* **12**, 4851-4868 (2000).
- 325 5. Tan, L. Z. *et al.* Shift current bulk photovoltaic effect in polar materials—hybrid and oxide perovskites
326 and beyond. *npj Computational Materials* **2**, 16026 (2016).
- 327 6. Young, S. M. & Rappe, A. M. First principles calculation of the shift current photovoltaic effect in
328 ferroelectrics. *Phys. Rev. Lett.* **109**, 116601 (2012).
- 329 7. Wang, F., Young, S. M., Zheng, F., Grinberg, I. & Rappe, A. M. Substantial bulk photovoltaic effect
330 enhancement via nanolayering. *Nat. Commun.* **7**, 10419 (2016).
- 331 8. Rangel, T. *et al.* Large bulk photovoltaic effect and spontaneous polarization of single-layer
332 monochalcogenides. *Phys. Rev. Lett.* **119**, 067402 (2017).
- 333 9. Cook, A. M., M. Fregoso, B., de Juan, F., Coh, S. & Moore, J. E. Design principles for shift current
334 photovoltaics. *Nat. Commun.* **8**, 14176 (2017).
- 335 10. Morimoto, T., Nakamura, M., Kawasaki, M. & Nagaosa, N. Current-voltage characteristic and shot
336 noise of shift current photovoltaics. *Phys. Rev. Lett.* **121**, 267401 (2018).
- 337 11. Cao, J. *et al.* Extended mapping and exploration of the vanadium dioxide stress-temperature phase
338 diagram. *Nano Lett.* **10**, 2667-2673 (2010).
- 339 12. Sturman, B. I. & Fridkin, V. M. *Photovoltaic and photo-refractive effects in noncentrosymmetric
340 materials*. Vol. **8**, 1-238 (CRC Press, 1992).
- 341 13. Li, H. *et al.* From bulk to monolayer MoS₂: evolution of Raman scattering. *Adv. Funct. Mater.* **22**,
342 1385-1390 (2012).
- 343 14. Ferrari, A. C. *et al.* Raman spectrum of graphene and graphene layers. *Phys. Rev. Lett.* **97**, 187401
344 (2006).
- 345 15. Parker, J. H., Feldman, D. W. & Ashkin, M. Raman scattering by silicon and germanium. *Phys. Rev.*
346 **155**, 712-714 (1967).
- 347 16. Zhang, Y. J. *et al.* Enhanced intrinsic photovoltaic effect in tungsten disulfide nanotubes. *Nature* **570**,
348 349-353 (2019).
- 349 17. Astafiev, S., Fridkin, V. & Lazarev, V. The influence of the magnetic field on the linear bulk
350 photovoltaic current in piezoelectric semiconductor GaP. *Ferroelectrics* **80**, 251-254 (1988).
- 351 18. Zhang, G. *et al.* New high *T_c* multiferroics KBiFe₂O₅ with narrow band gap and promising photovoltaic
352 effect. *Sci. Rep.* **3**, 1265 (2013).
- 353 19. Osterhoudt, G. B. *et al.* Colossal mid-infrared bulk photovoltaic effect in a type-I Weyl semimetal. *Nat.
354 Mater.* **18**, 471-475 (2019).
- 355 20. Fridkin, V. M. & Rodin, A. I. Anomalous photovoltaic effect in ferroelectric SbSI and cubic
356 piezoelectric ZnS. *Phys. Status Solidi A* **61**, 123-126 (1980).
- 357 21. Zenkevich, A. *et al.* Giant bulk photovoltaic effect in thin ferroelectric BaTiO₃ films. *Phys. Rev. B* **90**,
358 161409 (2014).
- 359 22. Glass, A. M., Linde, D. v. d. & Negran, T. J. High - voltage bulk photovoltaic effect and the
360 photorefractive process in LiNbO₃. *Appl. Phys. Lett.* **25**, 233-235 (1974).
- 361 23. Nadupalli, S., Kreisel, J. & Granzow, T. Increasing bulk photovoltaic current by strain tuning. *Sci. Adv.*
362 **5**, eaau9199 (2019).
- 363 24. Matsuo, H., Noguchi, Y. & Miyayama, M. Gap-state engineering of visible-light-active ferroelectrics
364 for photovoltaic applications. *Nat. Commun.* **8**, 207 (2017).

- 365 25. Ji, W., Yao, K. & Liang, Y. C. Evidence of bulk photovoltaic effect and large tensor coefficient in
366 ferroelectric BiFeO₃ thin films. *Phys. Rev. B* **84**, 094115 (2011).
- 367 26. Fridkin, V. M., Grekov, A. A. & Rodin, A. I. The bulk photovoltaic effect in the crystals without a
368 center of symmetry. *Ferroelectrics* **43**, 99-108 (1982).
- 369 27. Burger, A. M. *et al.* Direct observation of shift and ballistic photovoltaic currents. *Sci. Adv.* **5**, eaau5588
370 (2019).

371